Article

Molecular Basis of S100A1 Activation at Saturating and Subsaturating Calcium Concentrations

Caitlin E. Scott[1] and Peter M. Kekenes-Huskey[1,*]
[1]Department of Chemistry, University of Kentucky, Lexington, Kentucky

ABSTRACT The S100A1 protein mediates a wide variety of physiological processes through its binding of calcium (Ca^{2+}) and endogenous target proteins. S100A1 presents two Ca^{2+}-binding domains: a high-affinity "canonical" EF (cEF) hand and a low-affinity "pseudo" EF (pEF) hand. Accumulating evidence suggests that both Ca^{2+}-binding sites must be saturated to stabilize an open state conducive to peptide recognition, yet the pEF hand's low affinity limits Ca^{2+} binding at normal physiological concentrations. To understand the molecular basis of Ca^{2+} binding and open-state stabilization, we performed 100 ns molecular dynamics simulations of S100A1 in the apo/holo (Ca^{2+}-free/bound) states and a half-saturated state, for which only the cEF sites are Ca^{2+}-bound. Our simulations indicate that the pattern of oxygen coordination about Ca^{2+} in the cEF relative to the pEF site contributes to the former's higher affinity, whereas Ca^{2+} binding strongly reshapes the protein's conformational dynamics by disrupting β-sheet coupling between EF hands. Moreover, modeling of the half-saturated configuration suggests that the open state is unstable and reverts toward a closed state in the absence of the pEF Ca^{2+} ion. These findings indicate that Ca^{2+} binding at the cEF site alone is insufficient to stabilize opening; thus, posttranslational modification of the protein may be required for target peptide binding at subsaturating intracellular Ca^{2+} levels.

INTRODUCTION

S100A1 is a Ca^{2+}-binding protein commonly found in neuronal, renal (1), and cardiac (2,3) tissue, in the latter of which it is implicated in cardiomyopathy (for reviews, see (4,5)). S100A1 contributes to a variety of protein-protein interaction (PPI) events after Ca^{2+}-dependent activation, including those of the sarcoplasmic reticulum (ryanodine receptor (6,7), SERCA2a and phospholamban (8,9), and a cationic channel (TRPM3 (3)) to regulate Ca^{2+} homeostasis (10). The S100A1 protein forms a globular homodimer that contains two Ca^{2+}-binding sites per monomer, as shown in Fig. 1. Each S100A1 monomer presents two Ca^{2+}-binding sites consisting of a helix-loop-helix secondary-structure motif that is commonly called the "EF hand" (11). The canonical form of the EF hand, which we refer to as the cEF hand, consists of 12 residues and is highly conserved in many Ca^{2+}-binding proteins, such as calmodulin (CaM) and troponin C (TnC) (12,13).

The S100A1 cEF region spans 12 residues between D62 and E73, whereas the second, "pseudo" EF hand (pEF), is unique to the S100 family and related proteins, with 14 residues bridging S19 to E32 (11,14). Experiments show that the first Ca^{2+} ion binds to the cEF with a dissociation constant, K_d, of 27–250 μM compared to a K_d of 250–16,700 μM for the pEF domain (15,16)). It is further believed that Ca^{2+} binding to pEF proceeds in a noncooperative fashion (15), but the structural basis of consecutive binding remains unclear.

Upon saturation of the S100A1 monomer with two Ca^{2+} ions, the protein undergoes a conformational change from a closed to an open state that is characterized by the exposure of hydrophobic residues between helices 3 (H3) and 4 (H4) (15,16) (see Fig. 1). It is the presentation of this open hydrophobic patch that promotes PPIs (17,18), in a fashion similar to PPI formation by the TnC (19–22) and CaM proteins (23–25). Nuclear magnetic resonance (NMR) studies have revealed atomic-resolution details of the S100A1 conformations in the apo (Ca^{2+}-free) (26–28), holo (Ca^{2+}-saturated) (16,29) (Fig. 1, *A* and *B*), and target-protein-bound states (6,17,18). An open question, however, is how S100A1 participates in peptide-binding events given that saturation of the cEF and pEF hands requires Ca^{2+} ion concentrations of 100–10,000 μM, whereas physiological intracellular Ca^{2+} rarely exceeds tens of micromolar Ca^{2+} in localized regions (30,31).

To answer this question, we characterized key physiochemical drivers of high-affinity Ca^{2+} binding and the stabilization of the open state in the apo and holo states using molecular simulations. We complemented these analyses with simulations of the "half-saturated" configuration, for which only the cEF site is Ca^{2+} bound, to investigate the relative stability of the open and closed states when the pEF hand is devoid of Ca^{2+} ions. To this end, we performed 100 ns molecular dynamics (MD) simulations of the apo

Submitted August 3, 2015, and accepted for publication December 14, 2015.
*Correspondence: pkekeneshuskey@uky.edu
Editor: Michael Feig.

0006-3495/16/03/1052/12
http://dx.doi.org/10.1016/j.bpj.2015.12.040

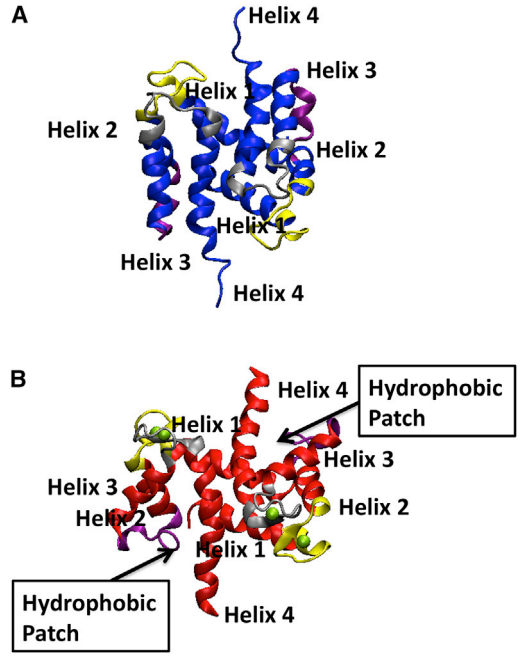

FIGURE 1 NMR structures of the human apo (PDB: 2L0P) (*A*) and holo (PDB: 2LP3) S100A1 (*B*) states (26,29). The pEF (*yellow*), linker (*purple*), cEF (*gray*), and helical bundle (*red*) are represented in the structures, and the Ca^{2+} ions (*green*) are shown for the holo form. The binding of Ca^{2+} ions reveals a hydrophobic protein recognition patch near H3. To see this figure in color, go online.

and holo states, as well as extended (>120 ns) runs on the half-saturated holo states to model the S100A1 structure and dynamics under physiological binding configurations. We relate the protein's Ca^{2+} and target-protein-binding mechanisms to structural dynamics local to the binding domains as well as to allosterically driven global conformational motions. First, we analyzed the binding site by estimating NMR amide order parameters as indicators of protein flexibility, for Ca^{2+}-binding domains in the apo and holo states. Second, we compared the relative positioning and coordination of EF-hand oxygens in the presence and absence of Ca^{2+} ion in the pEF and cEF hands. Third, we examined the impact of Ca^{2+}-ion binding on the global conformation of the protein through cross correlation, principal-component analysis (PCA), and measuring bundle helix displacements. Our results support prior experimental studies (15) suggesting that full EF-hand saturation is required for open-state stabilization. Hence, posttranslational modification of the protein may be required to form the open state for peptide recognition at physiological Ca^{2+} concentration levels. Moreover, our simulations provide, to our knowledge, new insight into 1) how chelating oxygen distributions and charges within the EF hands may tune Ca^{2+} binding affinities, and 2) the allosteric control of open-state stabilization via correlative motions and disruption of β-sheet formation between the cEF and pEF domains.

MATERIALS AND METHODS

MD simulations

NMR-derived homodimeric structures were used as starting conformations for the apo state (PDB: 2L0P (26) and 2LLU (28)), and holo state (PDB: 2LP3) (29). Using TLeap (32,33), all systems were neutralized, explicitly solvated in a 20.0-Å-margin TIP3P water box in 0.15 M KCl solution and parameterized with the AMBER-12SB force field (FF) (34). The protein consists of 186 residues in a system of ~20,000 water molecules and 130 neutralizing ions, for a total of ~60,000 atoms. Ca^{2+} parameters were based on a recent formulation for divalent ions (Li-Merz (35)) shown to reproduce experimental coordination numbers and hydration free energies through optimizing the cations' 12-6 Lennard Jones interactions (35). In the Results and Discussion section, we verify that the Li-Merz cation reasonably reproduces experimentally estimated coordination distances and EF-hand amide order parameters. Generally speaking, we have found that standard Ca^{2+} parameters, such as those from Marchand et al. (36), perform reasonably well for recapitulating coordinating structures and order parameters in EF-hand-based Ca^{2+}-binding proteins, including TnC (37,38). The PMEMD module within the AMBER 14 package (32,33) was used for minimization and equilibration, whereas the pmemd.cuda engines were used for the initial 100 ns production MD runs performed in quadruplicate. MD simulations in part utilized resources provided by the XSEDE high performance computing facilities (39). Our model of the half-saturated S100A1 was based on removing Ca^{2+} ions from the pEF hand of the holo structure (PDB: 2LP3); attempts to add Ca^{2+} ions to the apo state did not lead to an adequately coordinated structure. We recognize that the unresolved equilibrium conformations of the half-saturated state may entail localized reorganization of the protein; we approached this challenge by first performing normal equilibration routines to relax the EF-hand regions, followed by long-timescale MD simulations performed in succession. As discussed in the Results and Discussion section, significant relaxation of the protein toward an apo-like state was observed within 60 ns. We also performed four additional runs for snapshots from two of the half-saturated trajectories (see Section S1.3.6 in the Supporting Material). Further details of the MD simulation configurations are summarized in Section S1.1.1 in the Supporting Material).

Simulation trajectory analysis

Order parameters

Backbone N-H order parameters were calculated using the isotropic reorientational eigenmode dynamics approach (40) via the ptraj and mat2s2.py programs. Twenty scans consisting of window sizes of 5 ns (2500 frames) from the 100 ns (50,000 frames) saved for each simulation were used, which is comparable to the window sizes suggested by Genheden et al. (40).

Helix angles

Interhlx (K. Yap, University of Toronto, Toronto, Ontario, Canada) was used to calculate the interhelical angles. Helical lengths matched those from the respective NMR references and are outlined in Table S1. The helical angles were calculated for 500 snapshots saved every 0.2 ns during the 100 ns simulations.

Trajectory analysis and Ca^{2+}/oxygen radial distributions

Standard trajectory analyses including root mean square fluctuations (RMSFs), hydrogen-bonding patterns, and oxygen/Ca^{2+} distances were computed using the Lightweight Object-Oriented Structure library (LOOS) ((41) and T. D. Romo and A. Grossfield, 2013, *Biophys. J.*, abstract). Common reference positions were obtained by aligning the α-carbon atoms to the holo-state configuration (PDB: 2LP3 (29)). For Ca^{2+} coordination comparisons with the apo cases, the Ca^{2+} ion position was approximated by the corresponding location in the aligned holo state. Except where noted, all custom analyses were written in python and are available at https://bitbucket.org/pkhlab/pkh-lab-analyses/.

Electrostatic score

Two-dimensional histograms of the number of Ca^{2+}-oxygen contacts with respect to time and distance were computed for all side-chain oxygens and backbone oxygens to illustrate interactions between the Ca^{2+} ion and its oxygen ligands. We defined an electrostatic score (Eq. 1) to assess the interactions indicated in these histograms:

$$E_{\text{elec}} = q_{Ca^{2+}} \sum_{r_i} \sum_{j=\text{bb,sc}} \left(q_j \rho_j(r_i) r_i^{-1}\right), \quad (1)$$

where E_{elec} is the electrostatic score, $q_{Ca^{2+}}$ is the charge on the Ca^{2+} ion (+2), q_{bb} and q_{sc} are based on CHARMM partial charges for the backbone and side-chain oxygen atoms (−0.51 and −0.76, respectively) (42–44), and ρ is the density of oxygen atoms at distance r_i (Å). Although this formula resembles the Poisson model of electrostatic energy for a cloud of point charges, we opted for a simplified score given the difficulty of estimating a position-dependent dielectric constant in the neighborhood of the bound ion. The advantage of this approach is that we can qualitatively assess how the electrostatic field in the EF-hand domain changes between the apo and holo states. Conventional procedures for assessing interaction energies, such as molecular mechanics/Poisson Boltzmann surface area analysis (MM/PBSA) (45–48), are facilitated when an explicit Ca^{2+} ion is included in all simulations, which is unfeasible for the apo state. Nevertheless, to ensure that our electrostatic score was consistent with conventional interaction energy methods, we determined the MM electrostatic energies from the MM/PBSA program for the holo and half-saturated cases, as discussed in Section S1.2 in the Supporting Material.

PCA

The Bio3D package (49) was used to quantify the large-scale protein conformational changes shared by proteins homologous to S100A1, according to procedures we outlined for two related Ca^{2+}-binding proteins (see Kekenes-Huskey et al. (37) and Lindert et al. (38)). A BLAST search (50) on the human S100A1 sequence was performed with the NMR structure (PDB: 2L0P) (26) as input. Seven hundred and seventy-eight sequences were found, and the top 56 chains from 28 homodimer proteins with sequence identities ranging above 92.5% were used for subsequent sequence alignment and PCA. From these homologous sequences, Bio3D identified an invariant core of atoms with the least positional variation across all available protein structures. The invariant core most strongly consisted of those atoms buried within the S100A1 helical bundle. All structural sequences were aligned to this core, after which PCA was performed to identify bases presenting the largest modes of structural variation. The largest principal components (PCs) represent the most significant conformational differences between the apo and holo proteins; PCs 1 and 2 accounted for 74.4% of the variance, with PC1 making up 57.2% of the variance.

Residue cross correlation analysis

The four trajectories for each case were aligned using LOOS to both chains in the first frame of the respective NMR conformations. In Bio3D, residue cross correlation analysis was conducted with the dynamical cross correlation map (49,51,52) on the α-carbons of chain A (residues 1–93) for each protein.

RESULTS AND DISCUSSION

Predicted Ca^{2+}-coordination and N-H order parameters are consistent with NMR data

We first verified that our predicted coordination distances in the holo state are consistent with NMR-derived NOESY inter-proton distance constraints (29) (Table S2). The coordination distances in the simulations were measured between the specified atoms for every time step (2 fs) over the course of 100 ns, from which means and standard deviations were reported based on the averages for each independent simulation. The simulated data were compared against coordinating distances reflected in the ensemble of holo NMR structures (PDB: 2LP3 (29)). Nearly all average coordinating distances shown for the NMR structures were within 2.91 Å, compared to 2.77 Å in our simulations. One exception was the Ca^{2+}-N64 $O_{\delta 1}$ distance, for which we report an average distance of 4.26 ± 2.28 Å versus the NMR measured distances of 2.55 ± 0.04 Å. The larger standard deviation in our data reflects that the Ca^{2+}/N64 $O_{\delta 1}$ atoms were bound for a significant fraction of the simulation, although the Ca^{2+} ion would frequently exchange binding partners with water in the EF-hand domain. These data confirm that the Li-Merz Ca^{2+} parameter set reasonably reproduce experimentally determined coordination numbers and distances, despite their optimization for reproducing solvation structure and energies (35).

We next compared protein conformational dynamics reflected in our simulations with appropriate experimentally derived observables. Specifically, amide nitrogen/hydrogen order parameters have been widely used to probe backbone mobility in EF-hand-based proteins, particularly in the presence and absence of Ca^{2+} (29,53). By definition, order parameters approaching 1.0 signify greater protein rigidity, whereas order parameters approaching 0.0 imply greater flexibility. Order-parameter calculations thereby enable assessment of the Ca^{2+}-binding site and linker region stability, which can further be validated against experimental data. Specifically, prior NMR studies (29) of S100A1 in its apo and holo states indicated significant changes in backbone mobility, especially near the Ca^{2+}-binding region, where the presence of Ca^{2+} suppressed EF-hand fluctuations (leading to larger order parameters) relative to the apo state.

In Fig. 2, we compare prior NMR-derived order parameters with computed estimates averaged from four 100 ns simulations. In the three regions presented, the pEF hand (residues S19–E32; see Table S1), the linker (residues L41–D50), and the cEF hand (residues D62–E73), the estimates for the apo state are in good agreement with experiment (0.80 ± 0.01 theoretical versus 0.79 ± 0.02 experimental for pEF, 0.81 ± 0.01 versus 0.78 ± 0.02 for cEF, and 0.83 ± 0.02 versus 0.85 ± 0.03 for the linker). For the holo state, we note that the calculated order parameters were greater for the Ca^{2+}-binding sites relative to those calculated for the the apo state (0.85 ± 0.01 calculated holo versus 0.80 ± 0.01 calculated apo for the pEF and 0.84 ± 0.02 calculated holo versus 0.81 ± 0.01 calculated apo for the cEF), which signifies more rigid EF hands in the Ca^{2+}-bound state. The decreased mobility in the EF

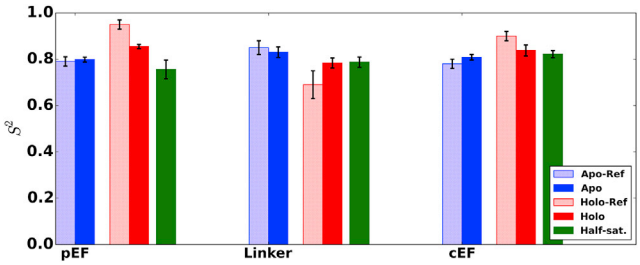

FIGURE 2 Experimental order parameters (29), S^2, for the apo (*light blue*) and holo (*light red*) cases versus the respective calculated order parameters (*dark blue* and *dark red*, respectively) and the calculated half-saturated cEF states (*green*). Vertical error bars represent standard deviations of the four averages of the two chains in each simulation. Predictions for the apo and holo states were consistent with experiment. To see this figure in color, go online.

holo state undoubtedly arises in part because the backbone and side-chain oxygens involved in coordinating Ca^{2+} are strongly bound and thus restrict backbone movement. We note, however, that our computed order parameters for the holo cases were similar to, but somewhat smaller than, the experimental holo measurements. This modest difference may suggest that our simulations moderately overestimated the lability of Ca^{2+}-binding regions. If this is the case, further refined Ca^{2+}/oxygen parameters (54) or use of polarizable force fields (55) may better stabilize coordination and recapitulate the order parameters derived from NMR studies. We nevertheless find agreement with the experimental trends for the linker region, residues 41–50, which suggest smaller order parameters for the holo state (calculated 0.78 ± 0.02) than for the apo state (calculated 0.83 ± 0.02). The holo state's smaller order parameters indicate greater linker mobility compared to the apo state, although the underlying mechanism is unclear.

The concurrence of our predicted order parameters and coordination distances with experiment suggest that the Li-Merz parameters are sufficiently reliable for predicting conformational and dynamic properties of small Ca^{2+}-binding proteins. These findings are also consistent with those of prior studies of similar globular Ca^{2+}-binding proteins, including TnC (37,38,56,57), CaM (58,59), and calbindin (36,60), which demonstrated good agreement with experimental measurements such as chelation distances, order parameters, and global conformational dynamics, using conventional MD protocols without polarization effects. Also remarkable were the results from Jiang et al. for Ca^{2+} binding to calbindin (60), for which the free energy of binding was within 2.1 kcal/mol of the experimental measurements. We note, however, that explicit consideration of polarization and charge transfer effects via ab initio methods (61) or polarizable models (45,55,62) are likely required for obtaining further refined estimates of protein/cation affinity. Validation of such methodologies and parameters may consider excellent experimental protein/cation affinity data such as those reported for CaM (63), for which site-specific affinity data were precisely measured. We nevertheless anticipate that subtle variation in chelation energetics due to these nonclassical phenomena would have limited impact on the chelation shell structure and global protein conformational dynamics, given the consistency of classical force-field MD simulations of Ca^{2+}-binding proteins with experimental probes of protein dynamics.

It has been reported (15) that at physiological Ca^{2+} concentrations, the pEF hand is not Ca^{2+} bound, and thus, the S100A1 open state is inaccessible. To provide insight into the backbone dynamics of the most probable binding configuration in physiological systems, we present order parameters for the half-saturated (cEF-only) S100A1 protein (see Fig. 2). Our calculated results indicate similar order parameters in the cEF region for the fully saturated holo and half-saturated systems (0.84 ± 0.02 and 0.82 ± 0.02, respectively), with modestly smaller order parameters for the latter configuration. Order parameters for the pEF region of the half-saturated state (0.76 ± 0.04) were comparable to and somewhat smaller than those reported for the unsaturated (apo) state (calculated as 0.80 ± 0.01) as opposed to the fully saturated holo state (calculated as 0.85 ± 0.01). The similarity of the pEF dynamics in the apo and half-saturated cases suggests that the presence of cEF-hand Ca^{2+} has little impact on the structure and mobility of the pEF region, which may support experimental observations of minimal Ca^{2+}-binding cooperativity (15). We find that the linker region is equally mobile in the half- and fully saturated configurations, which may indicate that the cEF-bound Ca^{2+} ion is sufficient to induce linker mobility.

In Section S1.3.2 in the Supporting Material, we present backbone amide nitrogen root mean-square fluctuations (RMSFs) for the apo, holo, and half-saturated states that quantify the relative lability of the EF-hand domains in a manner similar, but not equivalent, to the amide order parameters (Fig. S1). We find that in the pEF hand, the reported RMSFs were significantly greater for the apo and half-saturated proteins than for the holo states. This behavior was not unexpected, given that strong Ca^{2+}/oxygen interactions in the holo state should be expected to dampen pEF hand mobility. In the cEF hand, we note that the holo and half-saturated RMSFs were statistically comparable. Since the RMSF values merely indicate the relative fluctuations of the residues and not their positional decorrelation implied in order parameter analysis (64), these data indicate that the amides continued to fluctuate, although they were strongly constrained by the complexed Ca^{2+}.

Oxygen radial distribution about the bound Ca^{2+} ion

We further investigated the Ca^{2+} coordination to understand the molecular basis for higher Ca^{2+} affinity at the cEF

relative to the pEF hand (15). Canonical high-affinity EF-hand Ca^{2+} binding is typically afforded by short Ca^{2+}/oxygen distances (1.8–3.5 Å) stemming from seven oxygens arranged in a pentagonal bipyramidal fashion (12,13,65). In the cEF hand (D62–E73), the Ca^{2+} ion coordinated with seven oxygens, six of which were side-chain carboxylate oxygens and one backbone amide oxygen. The pEF hand (S19–E32) presented two additional residues relative to the cEF hand, which still promoted seven coordinate oxygens, although in this case, four arose from backbone oxygens, two from side-chain oxygens, and one from a bound water molecule (14). In Fig. 3, we report radial distributions of EF-hand oxygens within 12 Å of the coordinated Ca^{2+} position for the half-saturated and fully saturated holo states. For comparison, we also present data for the oxygen radial distribution in the apo state to demonstrate the substantial reorganization of coordinating ligands upon presentation of the Ca^{2+} ion. Fig. 3 *A* shows the oxygen population with respect to distance and time for the pEF and cEF hands, for which 7.0 is the optimal coordination number (11,14). For both pEF and cEF hands in the holo case, nearly optimal coordination at 2.5 Å is evidenced by a distinct red line that persists throughout the simulations. However, the cEF hand presents a higher degree of coordination, 6.45 ± 0.47, relative to the pEF hand, 5.32 ± 0.06. The nonintegral coordination number reflects the transient nature of Ca^{2+}/S100A1 oxygen binding owing to the rotation of side-chain carboxylate groups and exchange with bound solvent waters (not shown). Overall, the higher radial probability of coordinating oxygens for the cEF hand relative to pEF is consistent with the former's greater Ca^{2+} affinity.

The extent of EF-hand reorganization upon binding Ca^{2+} ions can be inferred from our apo-state data, for which the absence of Ca^{2+} ions permitted broadly and sparsely distributed chelating oxygens (see Fig. 3, *A* and *B*). Although this point of reference is biased toward the Ca^{2+}-bound configuration, it nevertheless illuminates the considerable mobility of the ligating oxygens. This behavior is consistent with the small order parameters reported in the EF-hand regions by Nowakowski et al. (29). For the half-saturated states, the reported cEF distribution is nearly coincident with the statistics observed in the holo configuration. In other words, the loss of the pEF Ca^{2+} ions has no apparent effect on the cEF coordinating oxygens, which may support prior experimental evidence suggesting that pEF and cEF bind Ca^{2+} noncooperatively (15). We note, however, that the half-saturated pEF-hand conformation significantly differed from that of the Ca^{2+}-free and fully saturated states, so we are unable to unambiguously define an approximate Ca^{2+} ion position for computing oxygen radial distributions. In the next section, we assess the approximate energetic stabilization due to these chelation patterns.

Calculated electrostatic scores based on chelating oxygens

The Ca^{2+} cation is anchored in the EF-hand binding site via electrostatic interactions with negatively charged oxygens, the resulting enthalpy of which likely dominates the binding free energy (66). To relate our simulated coordination geometries to an approximate electrostatic contribution to binding enthalpies, we introduce an "electrostatic score" that resembles Coulomb's law (Eq. 1). Similar to techniques applied to Ca^{2+}-binding channels, this score provides a simple metric for assessing the electrostatic potential from the chelating ions for both the Ca^{2+}-free- and Ca^{2+}-bound-state

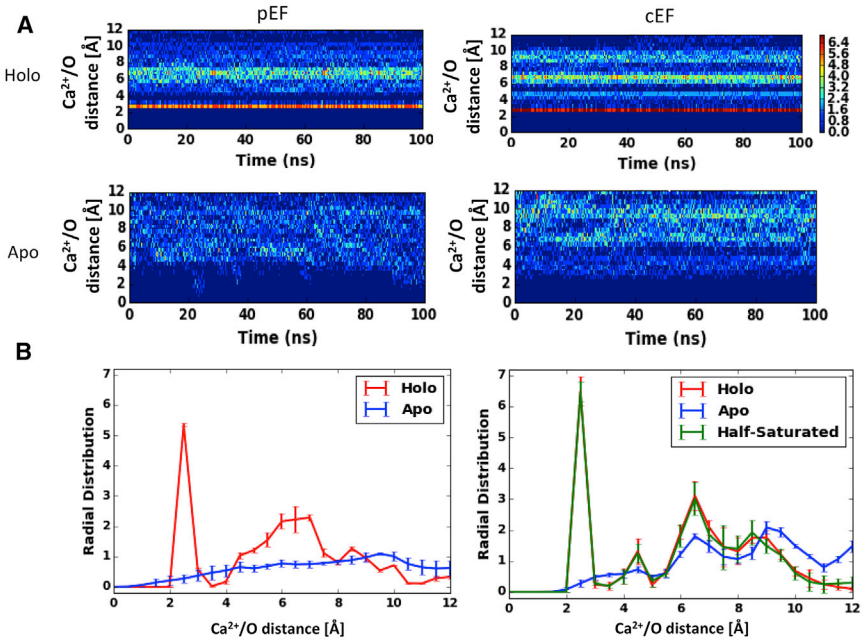

FIGURE 3 Time-dependent Ca^{2+}/oxygen distances (*A*) and averaged radial distribution of oxygen/Ca^{2+} (*B*) for the pEF (*left*) and cEF (*right*) hands. Vertical error bars indicate the mean ± SD of all four runs. Ca^{2+} binding localizes chelating oxygens to an ~2.5-Å-radius coordination shell. To see this figure in color, go online.

protein/cation interactions (67). We note that the higher negative partial charge in the coordinating side-chain carboxylic acid oxygens relative to backbone amide oxygens should lead to more favorable scores for the cEF versus pEF coordination. Indeed, the holo state cEF hand reports a more favorable average electrostatic score than the pEF hand by 1.46 units (pEF, −5.87 ± 0.04; cEF: −7.33 ± 0.29), as shown in Fig. 4 *A*, which is consistent with experimental binding trends. In Fig. 4 *B* and Section S1.3.3 in the Supporting Material, we show that the difference in electrostatic scores narrowed when all oxygens were assumed to share the same partial charge, as is assumed in some models (68). Hence, although it is understood that the positions of coordinating ligands are important determinants of Ca^{2+} affinity (12,13,65), these data indicate that oxygen partial charges and potentially mobilities further tune affinity. Although this electrostatic score assessment is simplistic, it captures the predominant electrostatic enthalpic contribution to the binding free energy and has a consistent trend with MM electrostatic interaction energies determined directly from AMBER MM/PBSA analysis (see Section S1.3.4 in the Supporting Material).

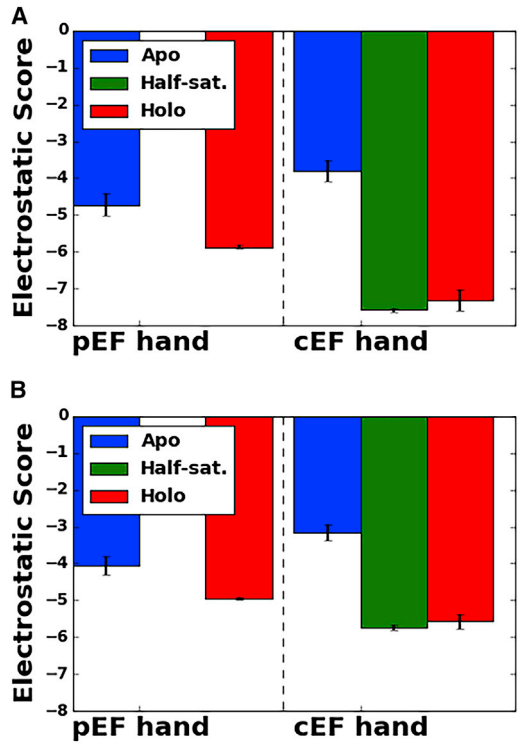

FIGURE 4 Electrostatic scores for the apo (*blue*), half-saturated (*green*), and fully saturated holo (*red*) states averaged over quadruplicate simulations. Results are given assuming partial charges of −0.51 and −0.76 on side-chain and backbone oxygens (*A*) versus uniform charges of −0.51 for both oxygen types (*B*). Vertical error bars indicate the mean ± SD of the eight electrostatic scores for two protein chains and four simulation runs. The higher density of coordinating oxygens and more negative partial charges in the cEF hand yield more stabilizing scores than for the pEF hand. To see this figure in color, go online.

We additionally computed the electrostatic score based on the apo state conformation to assess the gain in favorable enthalpic interactions as the protein relaxes in the presence of Ca^{2+} ions to form optimal binding interactions. As in the previous section, we present data for the apo state centered about the approximate position the Ca^{2+} ion would assume upon binding, to demonstrate the considerable change in the electrostatic environment upon chelating Ca^{2+}. Given comparable electrostatic scores for the apo states of the pEF and cEF hands (−4.72 ± 0.32 and −3.80 ± 0.30, respectively), Ca^{2+} ion binding yields greater reorganization energy for the latter, as holo state scores were 1.15 and 3.53 units more negative, respectively. Similar to our analysis of oxygen radial distributions in the previous section, we find that the electrostatic score for the Ca^{2+}-bound cEF hand in the half-saturated state (−7.58 ± 0.07) is nearly indistinguishable from that in the fully saturated holo state and further supports lack of cooperativity in pEF Ca^{2+} binding (15). However, there remains the possibility that the Ca^{2+}-bound cEF site preorganizes the pEF hand to facilitate rapid Ca^{2+} ion association rates, as we speculated previously for the EF hand in TnC mutants (37). Moreover, significant entropic contributions from coordinating oxygen desolvation and conformational reorganization will understandably contribute to the overall observed affinity (14). Although it is beyond the scope of this study, rigorous approaches for deriving binding free energies, such as free-energy perturbation or thermodynamic integration, could potentially help quantify these effects (47,69–71).

Stability of hydrogen bonds within the EF-hand β-sheets

To examine stabilizing contributions to the EF-hand regions, we calculated the average distance between the backbone amide nitrogen and oxygen atoms comprising β-sheets linking the pEF and cEF hands (Fig. 5). We observe that four hydrogen bonds, including K25-F71, K28-V69, K30-D67, and K31-G65 (polar heavy atom distances <3.5 Å), form

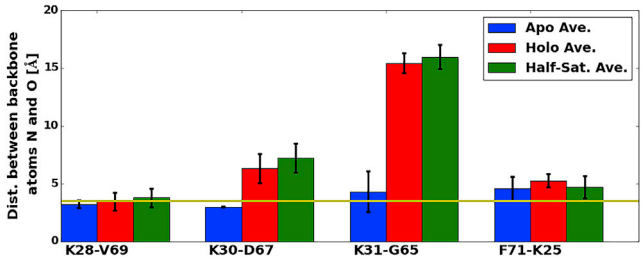

FIGURE 5 Average distances (Å) between backbone amide nitrogen and oxygen atoms of the residues in the EF hands forming the β-sheets in the apo case (*blue*), holo case (*red*), and half-saturated case (*green*). Standard deviations are shown. The yellow line indicates the 3.5 Å mark, which we define as the hydrogen-bond cutoff. Ca^{2+} ion binding disrupts the β-sheet hydrogen-bond network in both the half-saturated and holo states. To see this figure in color, go online.

within the β-sheets of the apo case, compared with only one in the holo case between K28 and V69. The larger degree of hydrogen bonding in the apo configuration likely helps stabilize the EF hand, which may help preorganize the binding site for Ca^{2+}-ion recognition (14). Meanwhile, the half-saturated case presents an intermediate degree of hydrogen bonding (two bonds, L28-V69 and K25-F71), which correlates with its order parameters. Notably, the largest change in the distance between two potential hydrogen-bond partners occurred between K31 and G65. In the apo state, they are separated by 4.33 $\pm$ 1.77 Å in the intact β-sheet secondary structure, but in the holo and half-saturated states, that distance increases to 15.43 $\pm$ 0.85 Å and 15.98 $\pm$ 1.04 Å, respectively, and thereby disrupt the β-sheet. As discussed further in Section S1.3.5 in the Supporting Material, we attribute this deviation to Ca^{2+} ion binding at the cEF hand. Specifically, N64 and D66 reorient to directly coordinate the Ca^{2+} ion, thereby pulling G65 away from active hydrogen bonding with residue K31 and compromising the β-sheet interaction. We will later present evidence that the disrupted β-sheet coupling upon Ca^{2+} binding directly correlates with increased mobility of helix 4 (H4), which together suggests that β-sheet hydrogen-bond breaking may trigger open-state formation.

Configuration and variability of the helix 3 and helix 4 angles

Ca^{2+} ion binding at the cEF and pEF hands is known to expose a hydrophobic PPI site between H3 and H4 (6,15–18). Interhelical angles have thus been commonly used (6,16,17,28,29,72) to assess the transition between open and closed states. Experimental studies (26,28,29) of the apo versus holo conformations have indicated significant interhelical angle changes between H1 and H3 ($-44.6 \pm 21.9°$ versus $-109.1 \pm 4.1°$ for the 2L0P apo and 2LP3 holo cases, respectively) and between H3 and H4 ($-166.6 \pm 1.7°$ versus $129.9 \pm 3.6°$ for the 2L0P apo and 2LP3 holo cases, respectively), culminating from the progression of H3 from closed to open states. Our helical angle measurements for the apo (Fig. 6) and holo states (Fig. 7) show excellent agreement between the simulation and the experiment. Namely, we observe for H3 and H4 that average values for the apo simulations are $-157.2 \pm 3.9°$ and $-150.4 \pm 7.3°$ versus $115.3 \pm 8.9°$ in the holo state. For the half-saturated case, the H3 and H4 angle approached $129.1 \pm 9.7°$, which is consistent with the holo state configuration. We will note in the subsequent section, however, that the half-saturated state fleetingly progresses toward an apo-like configuration characterized by closing of the H3/H4 angle. The comparatively sparse numbers and short durations of these excursions are apparently insufficient to significantly shift the interhelical angle average.

PCA of protein-recognition-site exposure

Ca^{2+} ion binding is known to expose the hydrophobic PPI site via migration of H3 toward an open-state configuration (17,18), which is accompanied by significant structural reorganization of the protein. To simplify interpretation of our simulations, we used PCA to project the protein's predominant conformational changes into a basis that clearly distinguished the apo from the holo states. The first two (largest eigenvalue) PCs for all S100A1 homologous structures available in the Protein Data Bank are shown in Fig. 8. In Fig. 8 *A*, we relate the PC bases to the conformational motions of the protein. PC1 is characterized by the swinging movement of H3 as it tilts outward from the apo state (26) toward the holo state (29) to allow room for binding peptides (6,18). PC2 is characterized by the unwinding of the H4 C-terminus (data not shown), though it is not clear whether this loss of helical secondary structure plays a role in tuning Ca^{2+} affinity in S100A1 variants. In Fig. 8 *B*, we demonstrate that the apo and holo structures are clearly separated by the first PC (PC1); specifically, the holo structures are localized to PC1 = -10 to -45 and the apo structures to PC1 = 5–40. We further find that S100A1 variants with higher Ca^{2+} ion affinity (for example, the holo rat S100A1 bound to the TRTK12 peptide) tend to have more positive PC2 values than those with weaker affinity. Similarly, two peptide-bound S100A1 rat protein structures with high

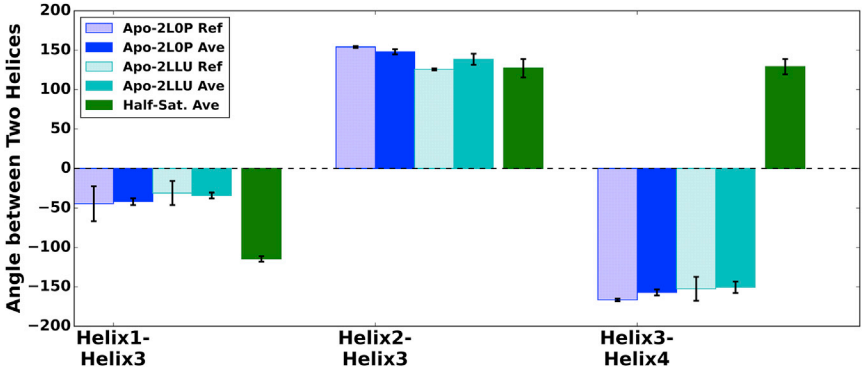

FIGURE 6 Computed versus experimental mean interhelical angles between H1 and H3, H2 and H3, and H3 and H4 for two apo NMR cases (PDB: 2L0P (*blue*) (26), 2LLU (*cyan*) (28)), and the half-saturated state (*green*). On average, the H1/H3 and H3/H4 angles in the half-saturated state are inconsistent with those in the apo state. To see this figure in color, go online.

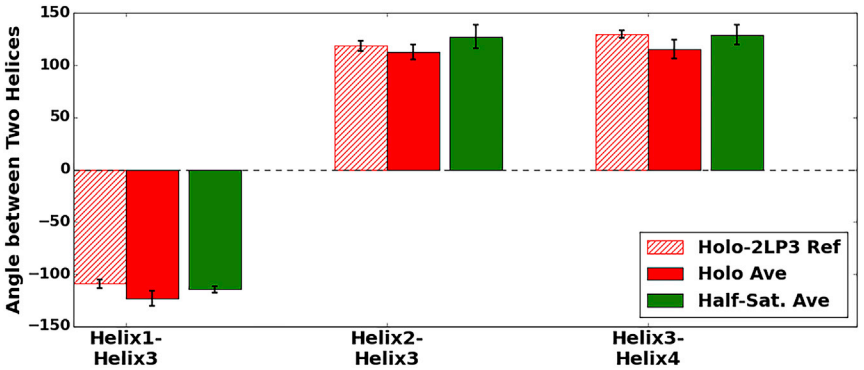

FIGURE 7 Computed (*solid*) versus experimental (*hatched*) mean interhelical angles between H1 and H3, H2 and H3, and H3 and H4 for one holo NMR case (PDB: 2LP3 (*red*) (29)) and the half-saturated state (*green*). On average, H1/H3 and H3/H4 angles in the half-saturated state are consistent with those in the holo state. To see this figure in color, go online.

Ca^{2+} ion affinity exhibit more positive PC2 values than the human holo state examined in this study.

Using these PCs, we show in Fig. 8 *B* the projections of the four MD trajectories of the apo, fully saturated holo, and half-saturated cases. For the apo case, the protein conformation samples PC2 extensively −27 to 27), but not PC1 (5–40), which suggests that the apo state remained in the closed configuration. Similarly, for the holo case, the trajectory is restricted to more negative PC1 values, indicating that the protein remains open. In contrast, the half-saturated state trajectories span a larger range of PC1 values, suggesting occasional excursions toward an apo-like closed state.

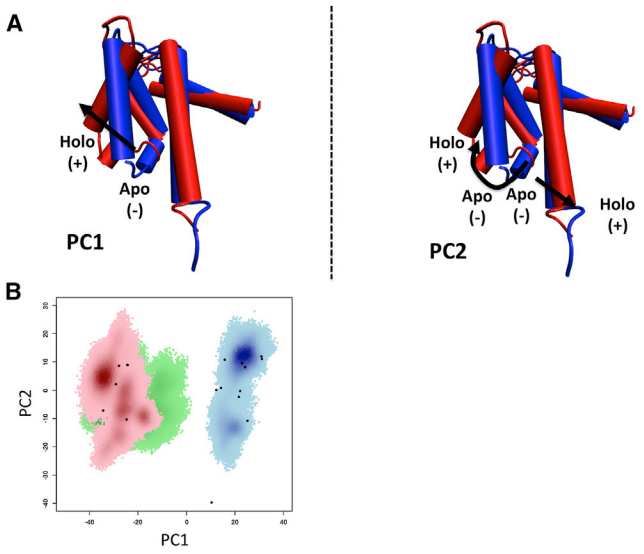

FIGURE 8 (*A*) PC1 (*left*) and PC2 (*right*) compared against the NMR structures of the human apo protein (*blue*; PDB: 2L0P) (26) and the human holo protein (*red*; PDB: 2LP3) (29). Movement of the respective PCs is in the direction from apo, indicated by (−), to holo, indicated by (+), as shown by the black arrows. PC1 is characterized by the swinging of the third helix away from the helical bundle. PC2 is characterized by the rotation of the third helix and the tilting of the fourth helix, both away from the helical bundle. (*B*) PCA for the four MD trajectories of the apo (*blue*), holo (*red*), and half-saturated (*green*) proteins, with NMR structures indicated as black dots. The half-saturated system samples intermediate regions along PC1 between the apo and holo states. To see this figure in color, go online.

To investigate the hypothesis that the removal of the pEF Ca^{2+} ions may prompt relaxation from the open toward the closed state, we selected four snapshots from intermediate PC1 values for extended MD simulations. In Fig. 9, we compare a snapshot from one 100 ns extended simulation

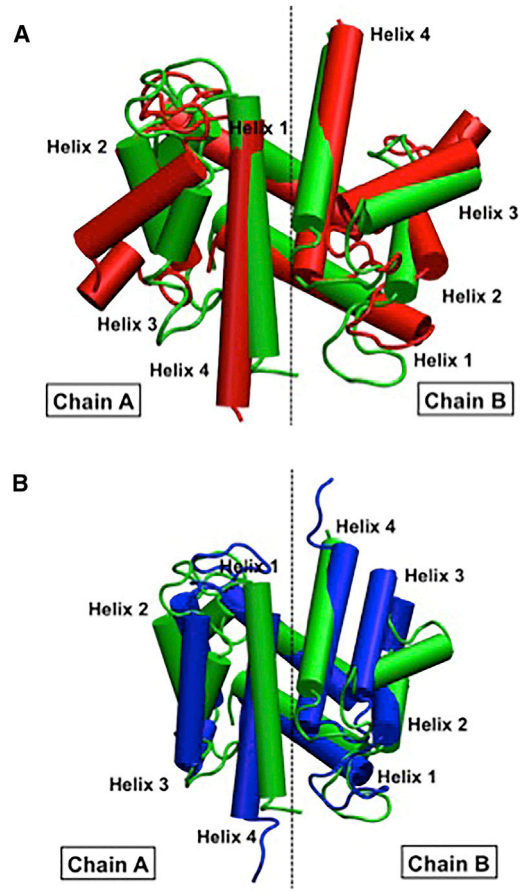

FIGURE 9 Comparison of a half-saturated S100A1 snapshot (*green*) extended for 100 ns beyond the initial 60 ns MD run against holo (*A*, *red*) and apo (*B*, *blue*) S100A1 structures (26,29). These half-saturated snapshots show a closer resemblance to the closed apo state; similar trends are reported for three other extended half-saturated simulations. To see this figure in color, go online.

with apo and holo S100A1 NMR structures (26,29). The snapshot indicates that the chain A H3 unwinds by several turns and tilts inward to closely resemble the apo NMR structure, whereas the chain B H3 maintains its original open position. Thus, it is apparent that in the absence of pEF Ca^{2+}ions, the open state may relax back to the closed state. Similar trends are reported in the other extended trajectories in Fig. S4. These results agree with data from Goch et al. (15) indicating that the hydrophobic patch was less solvent-exposed in subsaturating levels of Ca^{2+}. Overall, our data imply that the Ca^{2+} ion-bound pEF plays a critical role in stabilizing the holo-like state, despite its lesser affinity for Ca^{2+} ions relative to the cEF hand. Nevertheless, longer-duration MD simulations are likely required to fully repack H3 into the S100A1 helical bundle to more closely resemble the apo state. It is interesting to note that thiolation, glutathionylation, and nitrosylation of C85 on H4 has been suggested to increase Ca^{2+} binding affinity and induce significant conformational changes in the protein (15,28,72). Although few chemically modified C85 structures have been resolved, an attractive hypothesis is that covalently modified C85 could prevent H3 and H4 from fully closing, thereby producing a semiopen state that facilitates target peptide binding in the absence of pEF Ca^{2+} ions.

Cross-correlation analysis of interresidue coupling

Ca^{2+} ion binding at the pEF site (formed from H1 and H2) appears to modulate the H3 position, despite the fact that H3 and H4 are bridged by the cEF hand. This behavior is a hallmark of allostery, for which substrate binding induces protein conformational changes distal to the recognition region. A prominent hypothesis for allostery evokes the notion that long-range correlations between a binding site and distal regions of the protein (73) are involved in transferring the binding signal. We therefore report in Fig. 10 the cross correlation of Cα atom positions to uncover potential trends in this allosteric mechanism.

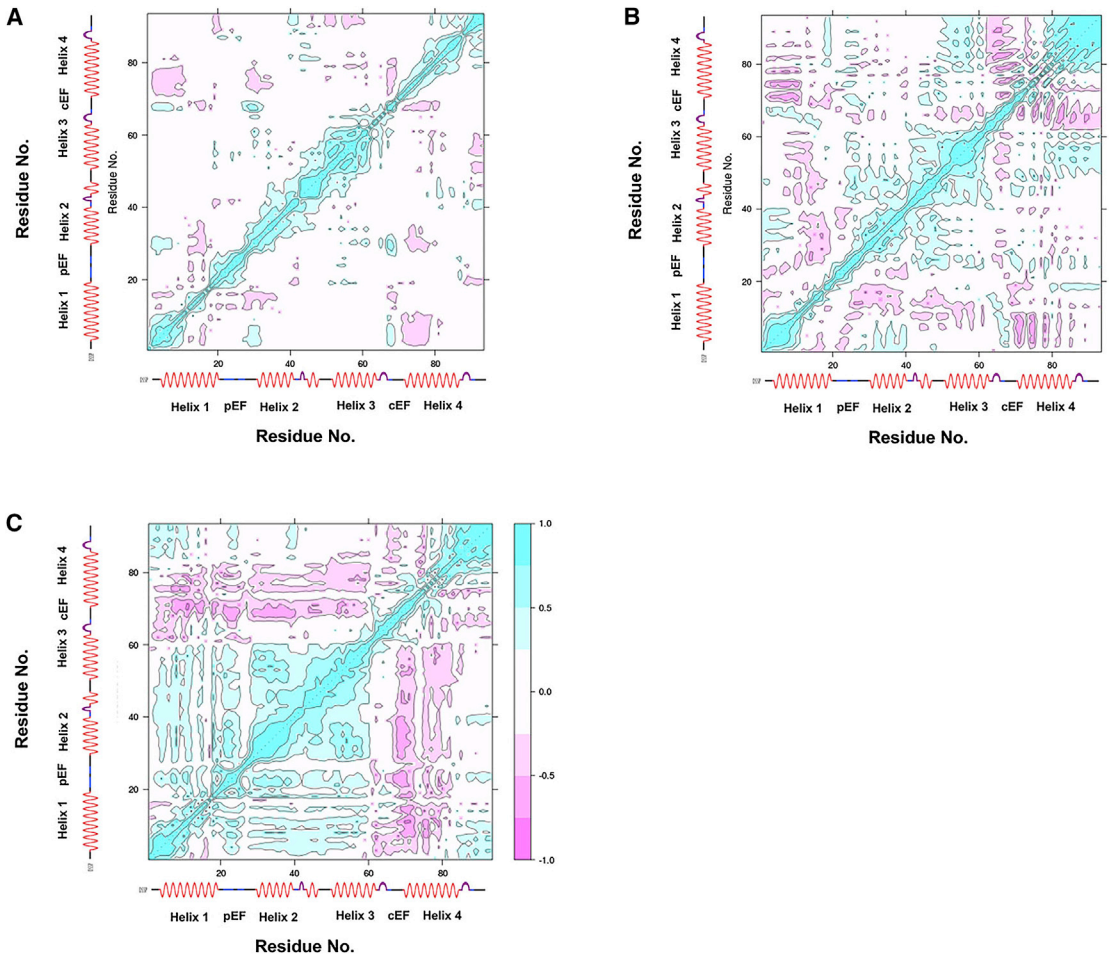

FIGURE 10 Residue cross correlation analysis for the human S100A1 protein in the apo (*A*), half-saturated (*B*), and holo (*C*) states. Cyan regions represent positive correlation, and magenta regions represent negative or anticorrelation. The half-saturated case presents correlation structure intermediate to the apo and holo cases. To see this figure in color, go online.

For the apo state (Fig. 10 *A*), we observe a small number of anticorrelated residues arising from breathing (opening) motions of H4 with H1 and H2, as well as with the EF hands. We note, however, a distinct positive correlation approximately between residues K25–K30 and E68–F71. This region corresponds to the β-sheet that tightly couples the EF hands in the apo state (14). Beyond these correlations, minimal coupling between distal regions is apparent. In contrast, the holo state (Fig. 10 *C*) presents a rich variety of off-diagonal (distal) correlations that evidence strong coupling between distal regions of the protein. We observe strong positive correlations, for instance, between H2, the linker region, and H3, as well as between H1, the pEF, the linker, and H3. Moreover, the negative correlations involving cEF and H4 appear to be intensified in the holo state relative to the apo site, which is suggestive of a breathing motion near the hydrophobic patch. Our earlier observations of EF-hand β-sheet decoupling upon Ca^{2+} binding appear to abolish the positive correlation in the K25–K30/E68–F71 region reported in the apo state with anticorrelative motions. Since these negative correlations extend from the β-sheet over the entirety of H4, we speculate that the β-sheet decoupling is the allosteric driver of the open-state formation. We additionally note in Fig. 10 *C* that C85 was anticorrelated with H3 residues 55–60 in the holo state, which may serve as additional evidence that C85 functionalization could enhance decoupling of H3 from H4. Hence, the barrier to exposing the hydrophobic region may be reduced and thus obviate the binding of Ca^{2+} ions at the pEF site, in support of findings from Zhukov et al (72). Similar analysis applied to the half-saturated state (Fig. 10 *B*) yields correlations intermediate between those of the apo and holo states that are suggestive of partial progression toward those configurations. More sophisticated methodologies for analyzing allostery in proteins, such as the mutual-information (74) or transmission-pathway (75) approach, could potentially provide greater insight into the Ca^{2+}-driven allostery of open-state formation.

CONCLUSIONS

Our MD simulations of the human S100A1 protein reveal structural and dynamic details of Ca^{2+} binding at the EF hands and its influence in forming the protein's functionally active open state. Using a primitive electrostatic scoring function, we find that the higher density and more negative partial charges of the coordinating oxygens in the cEF hand relative to the pEF region correlate with the former's stronger affinity for Ca^{2+} ions. In a separate manuscript, we are extending our primitive electrostatic score to include enthalpic and entropic terms to better quantify these affinities. We further find that in the absence of Ca^{2+} ion binding at the pEF hand, S100A1 appears to revert to an apo-like closed configuration whereby anticorrelation between H4 and the helical bundle in the holo state is diminished. We believe this transition is afforded by decoupling β-sheets linking the EF hands upon Ca^{2+} ion binding. Finally, the evident role of H4 in the transition between the apo and holo states appears consistent with reports of enhanced signaling propensity for chemically modified H4 C85 variants at subsaturating levels of Ca^{2+}. This insight into the molecular basis of high-affinity Ca^{2+} binding and its impact on allostery in S100A1 will be invaluable for understanding the function of the broad family of S100A-class proteins.

SUPPORTING MATERIAL

Supporting Materials and Methods, Supporting Results, four figures, and three tables are available at http://www.biophysj.org/biophysj/supplemental/S0006-3495(16)00050-3.

AUTHOR CONTRIBUTIONS

C.E.S. designed the research, performed the research, analyzed the data, and wrote the article. P.K.H. designed the research, analyzed the data, and wrote the article.

ACKNOWLEDGMENTS

P.K.H. thanks Jeff Wereszczynski for many helpful discussions. C.E.S. and P.K.H. thank Jason Swails and Kenneth Merz for their advice and help.

This work used the Extreme Science and Engineering Discovery Environment (XSEDE), which is supported by National Science Foundation grant number ACI-1053575.

SUPPORTING CITATIONS

References (76–80) appear in the Supporting Material.

REFERENCES

1. Zimmer, D. B., J. Chessher, …, W. E. Zimmer. 1997. S100A1 and S100B expression and target proteins in type I diabetes. *Endocrinology.* 138:5176–5183.
2. Kato, K., and S. Kimura. 1985. S100ao (α-α) protein is mainly located in the heart and striated muscles. *Biochim. Biophys. Acta.* 842:146–150.
3. Haimoto, H., and K. Kato. 1988. S100A0 (α-α) protein in cardiac muscle: isolation from human cardiac muscle and ultrastructural localization. *Eur. J. Biochem.* 171:409–415.
4. Kraus, C., D. Rohde, …, P. Most. 2009. S100A1 in cardiovascular health and disease: closing the gap between basic science and clinical therapy. *J. Mol. Cell. Cardiol.* 47:445–455.
5. Rohde, D., J. Ritterhoff, …, P. Most. 2010. S100A1: a multifaceted therapeutic target in cardiovascular disease. *J. Cardiovasc. Transl. Res.* 3:525–537.
6. Wright, N. T., B. L. Prosser, …, D. J. Weber. 2008. S100A1 and calmodulin compete for the same binding site on ryanodine receptor. *J. Biol. Chem.* 283:26676–26683.
7. Prosser, B. L., E. O. Hernandez-Ochoa, and M. F. Schneider. 2011. S100A1 and calmodulin regulation of ryanodine receptor in striated muscle. *Cell Calcium.* 50:323–331.
8. Kiewitz, R., C. Acklin, …, C. W. Heizmann. 2003. Ca^{2+}-dependent interaction of S100A1 with the sarcoplasmic reticulum Ca^{2+}-ATPase2a

and phospholamban in the human heart. *Biochem. Biophys. Res. Commun.* 306:550–557.

9. Most, P., A. Remppis, …, R. H. A. Fink. 2003. The C terminus (amino acids 75–94) and the linker region (amino acids 42–54) of the Ca^{2+}-binding protein S100A1 differentially enhance sarcoplasmic Ca^{2+} release in murine skinned skeletal muscle fibers. *J. Biol. Chem.* 278:26356–26364.
10. Duarte-Costa, S., R. Castro-Ferreira, …, A. F. Leite-Moreira. 2014. S100A1: a major player in cardiovascular performance. *Physiol. Res.* 63:669–681.
11. Grabarek, Z. 2006. Structural basis for diversity of the EF-hand calcium-binding proteins. *J. Mol. Biol.* 359:509–525.
12. Yang, J. J., A. Gawthrop, and Y. Y. Ye. 2003. Obtaining site-specific calcium-binding affinities of calmodulin. *Protein Pept. Lett.* 10:331–345.
13. Kirberger, M., X. Wang, …, J. J. Yang. 2008. Statistical analysis of structural characteristics of protein Ca^{2+}-binding sites. *J. Biol. Inorg. Chem.* 13:1169–1181.
14. Gifford, J. L., M. P. Walsh, and H. J. Vogel. 2007. Structures and metal-ion-binding properties of the Ca^{2+}-binding helix-loop-helix EF-hand motifs. *Biochem. J.* 405:199–221.
15. Goch, G., S. Vdovenko, …, A. Bierzynski. 2005. Affinity of S100A1 protein for calcium increases dramatically upon glutathionylation. *FEBS J.* 272:2557–2565.
16. Wright, N. T., K. M. Varney, …, D. J. Weber. 2005. The three-dimensional solution structure of Ca^{2+}-bound S100A1 as determined by NMR spectroscopy. *J. Mol. Biol.* 353:410–426.
17. Wright, N. T., B. R. Cannon, …, D. J. Weber. 2009. Solution structure of S100A1 bound to the CapZ peptide (TRTK12). *J. Mol. Biol.* 386:1265–1277.
18. Wright, N. T., Morgan, M. T., Cannon, B. R., K. M. Varney, and D. J. Weber. 2008. Solution structure of Ca-S100A1-TRTK12. http://www.rcsb.org/pdb/explore.do?structureId=2kbm. Accessed February 4, 2016.
19. Herzberg, O. J. M., and J. Moult. 1986. A model for the Ca^{2+}-induced conformational transition of troponin C. A trigger for muscle contraction. *J. Biol. Chem.* 261:2638–2644.
20. Houdusse, A., M. L. Love, …, C. Cohen. 1997. Structures of four Ca^{2+}-bound troponin C at 2.0 Å resolution: further insights into the Ca^{2+}-switch in the calmodulin superfamily. *Structure.* 5:1695–1711.
21. Strynadka, N. C. J., M. Cherney, …, M. N. G. James. 1997. Structural details of a calcium-induced molecular switch: x-ray crystallographic analysis of the calcium-saturated N-terminal domain of troponin C at 1.75 Å resolution. *J. Mol. Biol.* 273:238–255.
22. Wang, Z. Y., J. Gergely, and T. Tao. 1992. Characterization of the Ca^{2+}-triggered conformational transition in troponin C. *Proc. Natl. Acad. Sci. USA.* 89:11814–11817.
23. Finn, B. E., T. Drakenberg, and S. Forsen. 1993. The structure of apo-calmodulin. A ^{1}H NMR examination of the carboxy-terminal domain. *FEBS Lett.* 336:368–374.
24. Finn, B. E., J. Evenas, …, S. Forsen. 1995. Calcium-induced structural changes and domain autonomy in calmodulin. *Nat. Struct. Biol.* 2:777–783.
25. Tan, R. Y., Y. Mabuchi, and Z. Grabarek. 1996. Blocking the Ca^{2+}-induced conformational transitions in calmodulin with disulfide bonds. *J. Biol. Chem.* 271:7479–7483.
26. Nowakowski, M., L. Jaremko, …, A. Ejchart. 2011. Solution NMR structure and dynamics of human apo-S100A1 protein. *J. Struct. Biol.* 174:391–399.
27. Rustandi, R. R., D. M. Baldisseri, …, D. J. Weber. 2002. Three-dimensional solution structure of the calcium-signaling protein Apo-S100Al as determined by NMR. *Biochemistry.* 41:788–796.
28. Zivkovic, M. L., M. Zareba-Koziol, …, A. Wyslouch-Cieszynska. 2012. Post-translational S-nitrosylation is an endogenous factor fine tuning the properties of human S100A1 protein. *J. Biol. Chem.* 287:40457–40470.
29. Nowakowski, M., K. Ruszczynska-Bartnik, …, A. Ejchart. 2013. Impact of calcium binding and thionylation of S100A1 protein on its nuclear magnetic resonance-derived structure and backbone dynamics. *Biochemistry.* 52:1149–1159.
30. Berridge, M. J., P. Lipp, and M. D. Bootman. 2000. The versatility and universality of calcium signalling. *Nat. Rev. Mol. Cell Biol.* 1:11–21.
31. Shannon, T., F. Wang, …, D. Bers. 2004. A mathematical treatment of integrated Ca dynamics within the ventricular myocyte. *Biophys. J.* 87:3351–3371.
32. Pearlman, D. A., D. A. Case, …, P. Kollman. 1995. AMBER, A package of computer-programs for applying molecular mechanics, normal-mode analysis, molecular dynamics, and free energy calculations to simulate the structural and energetic properties of molecules. *Comput. Phys. Commun.* 91:1–41.
33. Case, D. A., T. E. Cheatham, …, R. J. Woods. 2005. The Amber biomolecular simulation programs. *J. Comput. Chem.* 26:1668–1688.
34. Cornell, W. D., P. Cieplak, …, P. A. Kollman. 1995. A second generation force field for the simulation of proteins, nucleic acids, and organic molecules. *J. Am. Chem. Soc.* 117:5179–5197.
35. Li, P. F., B. P. Roberts, …, K. M. Merz. 2013. Rational design of particle mesh Ewald compatible Lennard-Jones parameters for +2 metal cations in explicit solvent. *J. Chem. Theory Comput.* 9:2733–2748.
36. Marchand, S., and B. Roux. 1998. Molecular dynamics study of calbindin D9k in the apo and singly and doubly calcium-loaded states. *Proteins.* 33:265–284.
37. Kekenes-Huskey, P., S. Lindert, and J. McCammon. 2012. Molecular basis of calcium-sensitizing and desensitizing mutations of the human cardiac troponin C regulatory domain: a multi-scale simulation study. *PLOS Comput. Biol.* 8:e1002777.
38. Lindert, S., P. Kekenes-Huskey, …, J. McCammon. 2012. Dynamics and calcium association to the N-terminal regulatory domain of human cardiac troponin C: a multiscale computational study. *J. Phys. Chem. B.* 116:8449–8459.
39. Towns, J., T. Cockerill, …, N. Wilkens-Diehr. 2014. XSEDE: accelerating scientific discovery. *Comput. Sci. Eng.* 16:62–74.
40. Genheden, S., C. Diehl, …, U. Ryde. 2010. Starting-condition dependence of order parameters derived from molecular dynamics simulations. *J. Chem. Theory Comput.* 6:2176–2190.
41. Romo, T., and A. Grossfield. 2009. LOOS: An extensible platform for the structural analysis of simulations. *Conf. Proc. IEEE Eng. Med. Biol. Sci.* 2009:2332–2335.
42. Best, R. B., X. Zhu, …, A. D. MacKerell. 2012. Optimization of the additive CHARMM all-atom protein force field targeting improved sampling of the backbone ϕ, ψ and side-chain χ^1 and χ^2 dihedral angles. *J. Chem. Theory Comput.* 8:3257–3273.
43. MacKerell, A. D., M. Feig, and C. L. Brooks. 2004. Improved treatment of the protein backbone in empirical force fields. *J. Am. Chem. Soc.* 126:698–699.
44. MacKerell, A. D., D. Bashford, …, M. Karplus. 1998. All-atom empirical potential for molecular modeling and dynamics studies of proteins. *J. Phys. Chem. B.* 102:3586–3616.
45. Kollman, P. A., I. Massova, …, T. E. Cheatham. 2000. Calculating structures and free energies of complex molecules: combining molecular mechanics and continuum models. *Acc. Chem. Res.* 33:889–897.
46. Gohlke, H., and D. A. Case. 2004. Converging free energy estimates: MM-PB(GB)SA studies on the protein-protein complex Ras-Raf. *J. Comput. Chem.* 25:238–250.
47. Hou, T., J. Wang, …, W. Wang. 2011. Assessing the performance of the molecular mechanics/Poisson Boltzmann surface area and molecular mechanics/generalized Born surface area methods. II. The accuracy of ranking poses generated from docking. *J. Comput. Chem.* 32:866–877.
48. Miller, I., R. Bill, …, A. E. Roitberg. 2012. MMPBSA.py: an efficient program for end-state free energy calculations. *J. Chem. Theory Comput.* 8:3314–3321.

49. Grant, B. J., A. P. C. Rodrigues, …, L. S. D. Caves. 2006. Bio3d: an R package for the comparative analysis of protein structures. *Bioinformatics.* 22:2695–2696.

50. Altschul, S. F., T. L. Madden, …, D. D. J. Lipman. 1997. Gapped BLAST and PSI-BLAST: a new generation of protein database search programs. *Nucleic Acids Res.* 25:3389–3402.

51. McCammon, A. J., and S. C. Harvey. 1986. Dynamics of Proteins and Nucleic Acids. Cambridge University Press, Cambridge, United Kingdom.

52. Lange, O., and H. Grubmuller. 2006. Generalized correlation for biomolecular dynamics. *Proteins.* 62:1053–1061.

53. Spyracopoulos, L., P. Lavigne, …, B. D. Sykes. 2001. Temperature dependence of dynamics and thermodynamics of the regulatory domain of human cardiac troponin C. *Biochemistry.* 40:12541–12551.

54. Saxena, A., and D. Sept. 2013. Multisite ion models that improve coordination and free energy calculations in molecular dynamics simulations. *J. Chem. Theory Comput.* 9:3538–3542.

55. Kohagen, M., M. Lepšík, and P. Jungwirth. 2014. Calcium binding to calmodulin by molecular dynamics with effective polarization. *J. Phys. Chem. Lett.* 5:3964–3969.

56. Wang, D., I. M. Robertson, …, M. Regnier. 2012. Structural and functional consequences of the cardiac troponin C L48Q Ca^{2+}-sensitizing mutation. *Biochemistry.* 51:4473–4487.

57. Lindert, S., P. Kekenes-Huskey, and J. McCammon. 2012. Long-timescale molecular dynamics simulations elucidate the dynamics and kinetics of exposure of the hydrophobic patch in troponin C. *Biophys. J.* 103:1784–1789.

58. Yang, C., G. Jas, and K. Kuczera. 2004. Structure, dynamics and interaction with kinase targets: computer simulations of calmodulin. *Biochim. Biophys. Acta.* 1697:289–300.

59. Aykut, A. O., A. R. Atilgan, and C. Atilgan. 2013. Designing molecular dynamics simulations to shift populations of the conformational states of calmodulin. *PLOS Comput. Biol.* 9:e1003366.

60. Jiang, W., Y. Luo, …, B. Roux. 2012. Calculation of free energy landscape in multi-dimensions with Hamiltonian-exchange umbrella sampling on petascale supercomputer. *J. Chem. Theory Comput.* 8:4672–4680.

61. Biekofsky, R. R., A. G. Turjanski, …, A. Pastore. 2011. Ab initio study of NMR ^{15}N chemical shift differences induced by Ca^{2+} binding to EF-hand proteins. *Biochemistry.* 43:6554–6564.

62. Cieplak, P., F.-Y. Dupradeau, …, J. Wang. 2009. Polarization effects in molecular mechanical force fields. *J. Phys. Condens. Matter.* 21:333102.

63. Ye, Y., H. W. Lee, …, S. Shealy. 2005. Probing site-specific calmodulin calcium and lanthanide affinity by grafting. *J. Am. Chem. Soc.* 127:3743–3750.

64. Lipari, G., and A. Szabo. 1982. Model-free approach to the interpretation of nuclear magnetic resonance relaxation in macromolecules. 1. Theory and range of validity. *J. Am. Chem. Soc.* 104:4546–4559.

65. Maniccia, A. W., W. Yang, …, J. J. Yang. 2009. Inverse tuning of metal binding affinity and protein stability by altering charged coordination residues in designed calcium binding proteins. *PMC Biophys.* 2:11.

66. Ben-Amotz, D., and R. Underwood. 2008. Unraveling water's entropic mysteries: a unified view of nonpolar, polar, and ionic hydration. *Acc. Chem. Res.* 41:957–967.

67. Nonner, W., D. Gillespie, …, B. Eisenberg. 2001. Ion accumulation in a biological calcium channel: effects of solvent and confining pressure. *J. Phys. Chem. B.* 105:6427–6436.

68. Nonner, W., L. Catacuzzeno, and B. Eisenberg. 2000. Binding and selectivity in L-type calcium channels: a mean spherical approximation. *Biophys. J.* 79:1976–1992.

69. Beard, H., A. Cholleti, …, K. A. Loving. 2013. Applying physics-based scoring to calculate free energies of binding for single amino acid mutations in protein-protein complexes. *PLoS One.* 8:1–11.

70. Lindert, S., Y. H. Cheng, …, J. A. McCammon. 2015. Effects of HCM cTnI mutation R145G on troponin structure and modulation by PKA phosphorylation elucidated by molecular dynamics simulations. *Biophys. J.* 108:395–407.

71. Zou, X., Y. Sun, and I. D. Kunz. 1999. Inclusion of solvation in ligand binding free energy calculations using the generalized-Born model. *J. Am. Chem. Soc.* 121:8033–8043.

72. Zhukov, I., A. Ejchart, and A. Bierzynski. 2008. Structural and motional changes induced in apo-S100A1 protein by the disulfide formation between its Cys 85 residue and β-mercaptoethanol. *Biochemistry.* 47:640–650.

73. Long, D., and R. Bruschweiler. 2011. Atomistic kinetic model for population shift and allostery in biomolecules. *J. Am. Chem. Soc.* 133:18999–19005.

74. McClendon, C. L., G. Friedland, …, M. P. Jacobson. 2009. Quantifying correlations between allosteric sites in thermodynamic ensembles. *J. Chem. Theory Comput.* 5:2486–2502.

75. Van Wart, A. T., J. Durrant, …, R. E. Amaro. 2014. Weighted implementation of suboptimal paths (WISP): an optimized algorithm and tool for dynamical network analysis. *J. Chem. Theory Comput.* 10:511–517.

76. Miyamoto, S., and P. A. Kollman. 1992. SETTLE: an analytical version of the SHAKE and RATTLE algorithm for rigid water models. *J. Comput. Chem.* 13:952–962.

77. Ryckaert, J. P., G. Ciccotti, and H. J. C. Berendsen. 1977. Numerical integration of cartesian equations of motion of a systerm with constraints: molecular dynamics of N-alkanes. *J. Comput. Phys.* 23:327–341.

78. Berendsen, H. J. C., J. P. M. Postma, …, J. R. Haak. 1984. Molecular dynamics with coupling to an external bath. *J. Chem. Phys.* 81:3684–3690.

79. Darden, T., D. York, and L. Pedersen. 1993. Particle mesh Ewald: an N.log(N) method for Ewald sums in large systems. *J. Chem. Phys.* 98:10089–10092.

80. Case, D., V. Babin, …, P. A. Kollman. 2014. AMBER 14. University of California, San Francisco, CA.

Biophysical Journal, Volume *110*

Supplemental Information

Molecular Basis of S100A1 Activation at Saturating and Subsaturating Calcium Concentrations

Caitlin E. Scott and Peter M. Kekenes-Huskey

1 Supplement

1.1 Methods

1.1.1 Molecular dynamics setup

In addition to the general setup protocol for the molecular simulations explained in the Methods section, we provide the following configuration details. Covalent bonds containing hydrogen atoms were constrained by the SHAKE algorithm, thus justifying the use of a 2 fs time step for all trials (1, 2). Periodic boundary conditions (PBC) were applied during all minimization and dynamics steps. Minimization consisted of 1000 steps with the protein held fixed with restraints of 500.0 kcal/(mol $\mathring{A}^2$) using steepest descent and conjugate gradient optimization methods. This step was followed by 5000 steps of minimization, using the same scheme except with all the atoms movable. For the molecular dynamics runs, the Berendsen thermostat and barostat (for constant pressure simulations) were used (3), while non-bonding interactions were calculated using the particle mesh Ewald (PME) method (4) with a cut-off of 10 Å. The first equilibration step entailed heating the waters and counter ions with the protein fixed via the AMBER belly command from 0 to 300 K for the first 0.08 ns before being held at a constant temperature of 300 K for the final 0.02 ns of the MD constant volume simulations. This simulation was followed by heating the entire system with all atoms movable from 0 to 300 K for the first 0.4 ns before running at a constant 300 K for the remaining 0.1 ns of the 0.5 ns NVT MD. The final equilibration step was a 1 ns MD NPT run at 300 K and 1 bar with everything movable with a pressure relaxation time of 2.0 ps. For the production runs, the atoms' velocities were randomly initialized, and the simulations were conducted with a 2 fs time step at a constant temperature of 300 K and a constant pressure of 1.0 bar with a 2.0 ps pressure relaxation time.

Minimization and early steps of equilibration were conducted on 3.60 GHz Intel Core i7-3820 central processing units (CPUs). The production simulations were run on graphical processing units (GPUs) GeForce GTX 780 with driver

version: 346.59 or on the 2.6 GHz Intel EM64T Xeon E5 CPUs on the XSEDE supercomputer SDSU Gordon Compute cluster.

1.2 Molecular mechanics electrostatic energy

For comparison and validation with our calculated electrostatic score (discussed above), we calculated the molecular mechanics electrostatic energy from the binding free energy resulting from the Ca^{2+} ion interacting with the residues in either the pEF or the cEF hand for the fully-saturated holo and half-saturated simulations. We used the molecular mechanics/Poisson Boltzmann surface area analysis (MM/PBSA) program (5–8), which is part of the AMBER 14 package (9), to perform calculations on 100 snapshots corresponding to one snapshot per nanosecond sampled with the cpptraj program. The binding free energy, calculated by the MM/PBSA program, is defined as:

$$\begin{aligned} \Delta G_{bind} &= G_{complex} - G_{protein} - G_{ligand} \\ &= \Delta E_{MM} + \Delta G_{PB} + \Delta G_{nonpolar} - T\Delta S \end{aligned} \tag{S1}$$

where ΔE_{MM} is the change in the molecular mechanical energy (computed using the molecular dynamics engine), ΔG_{PB} is the change in the solvation free energy determined with the Poisson-Boltzmann equation, $\Delta G_{nonpolar}$ is the change in the non-polar free energy based on a surface area calculation, and $T\Delta S$ is the temperature of the simulation multiplied by the change in entropy. For comparison against our electrostatic score, we extracted the electrostatic contribution to ΔE_{MM}. Here, only the Ca^{2+} ion, acting as the ligand, and the 12 or 14 residues making up the respective EF hand, acting as the receptor, were included in the calculations. As reported in the main text for our electrostatic score, the holo state's cEF has a significantly more favorable electrostatic interaction energy than the pEF hand. This trend is verified by identical rankings based on MM electrostatic energies (see Fig. S2 and Table S3 in Section 1.3.4). Namely, for the holo case the interaction energy between the Ca^{2+} ion and the

residues in the cEF hand is more favorable by 409.1 kcal/mol than in the pEF hand. These data support that our electrostatic score is reliable and accurately reflects the trends shown in the MM electrostatic energies. However, an advantage of the electrostatic score is that we can qualitatively estimate the strength of electrostatic cases in cases lacking the Ca^{2+} ion (specifically the apo state and vacant pEF hand of the half-saturated state). This advantage permits the estimation of how reordering chelating oxygens in the holo state relative to the apo improves the Ca^{2+} electrostatic interaction energy.

1.3 Results

1.3.1 Region definitions and Ca^{2+} coordination

Table S1: Residue ranges for the S100A1 four alpha-helices.

Configuration	PDB ID	Helix 1	pEF	Helix 2	Helix 3	cEF	Helix 4
Apo	2L0P (10)	3-18	19-32	30-41	51-64	62-73	71-86
Apo	2LLU (11)	3-17	19-32	30-40	51-63	62-73	71-86
Holo	2LP3 (12)	3-20	19-32	30-40	53-61	62-73	71-91

1.3.2 RMSFs indicate the flexibility of various regions of the protein

RMSFs, like the order parameters, are indicators of protein flexibility. In previous work examining Ca^{2+} binding to the EF hand protein troponin C (TnC) (13, 14), we found that root-mean square fluctuations (RMSF) of the Ca^{2+} binding loop backbone carbons were comparable to the amide order parameters. We furthermore noted that one TnC mutant appeared to suppress backbone fluctuations in the apo state, which we argued explained the experimentally reduced Ca^{2+} association rates as minimal reorganization of the binding site was necessary to accommodate the Ca^{2+} ions. As discussed above, measurements of protein flexibility show the stabilizing force of the Ca^{2+} ion on the local and global protein structure. The trends in the RMSFs are expected to mirror those

Table S2: Holo state Ca^{2+}/oxygen coordination distances for experimental and simulated structures.

Coordinate oxygen	EF hand	NMR (PDB ID: 2LP3 (12)) [Å]	Simulated [Å]
S19 O	pEF	2.44 ± 0.04	2.36 ± 0.18
E22 O		2.44 ± 0.03	2.71 ± 1.02
D24 O		2.51 ± 0.04	2.56 ± 0.61
K27 O		2.46 ± 0.05	2.53 ± 0.42
E32 $O_{\epsilon 1}$		2.43 ± 0.19	2.25 ± 0.10
E32 $O_{\epsilon 2}$		2.80 ± 0.29	2.32 ± 0.11
E62 $O_{\delta 1}$	cEF	2.33 ± 0.41	2.49 ± 0.67
N64 $O_{\delta 1}$		2.55 ± 0.04	4.26 ± 2.28
D66 $O_{\delta 1}$		2.83 ± 0.33	2.27 ± 0.16
D66 $O_{\delta 2}$		2.41 ± 0.23	2.77 ± 0.63
E68 O		2.53 ± 0.04	2.31 ± 0.08
E73 $O_{\epsilon 1}$		2.69 ± 0.37	2.35 ± 0.42
E73 $O_{\epsilon 2}$		2.91 ± 0.57	2.36 ± 0.19

of the experimental order parameters in Fig. S1. For example, we expect the pEF and cEF hands in the apo protein to be more flexible than those of the holo protein since they lack the Ca^{2+} ions to orient the protein structure. However, in the linker region, we expect the apo protein to be more stable as indicated by the experimental order parameters (12). As for the half-saturated state, we expect that the protein backbone would have a greater RMSF in the pEF and cEF regions. The Ca^{2+} ion is missing in the pEF hand, so the protein will not orient itself around it. But, we also expect that the pEF hand ion impacts the cEF because experiments indicate that both ions are necessary to obtain the holo state (15). Thus, we expect the pEF hand shape will affect that of the cEF. This hypothesis is reasonable since the pEF and cEF interact in the form of a β-sheet (see Fig. 1) .

Fig. S1 shows the amide nitrogen RMSF per residue averaged over two chains and four MD simulations. In the S100A1 protein, there are peaks in the RMSF values at residues 19-30 and 40-70. The former region corresponds to the pEF hand, residues S19 to E32. Of the three protein states examined here, the holo

protein had the smallest average RMSF over this region, peaking at 1.25 ± 0.47 Å followed by the apo protein at 2.27 ± 0.84 Å and the half-saturated protein at 2.68 ± 0.78 Å. This trend is appropriate because the holo protein is the only case that has a Ca^{2+} ion to coordinate the residues and thus stabilize the protein conformation. The other two cases lack the structural reinforcement provided by the ion. This trend also agrees with the order parameters shown in Fig. 2. According to the calculated values, the half-saturated state is the most flexible followed by the apo state then the holo one. And the experimental values show that the apo state is more flexible than the holo one at the pEF hand (12).

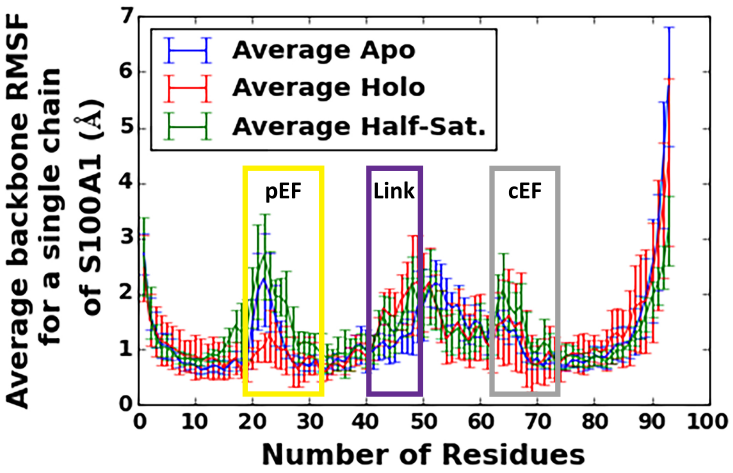

Figure S1: Backbone amide nitrogen RMSF per residue of the apo (blue), holo (red), and half-saturated (green) averaged over the two homo-dimer chains and the four MD runs. The pEF (yellow), linker (purple), and cEF (gray) regions are outlined.

The second region (residues E40 to D70) corresponds to the linker region at residues L41 to D50 and the cEF hand at residues D62 to E73. In the linker region, there is a steady increase in RMSF with increasing residue number. The holo and half-saturated cases consistently have RMSFs greater by 0.5 Å than the apo state, which agrees with the experimental and calculated order parameters that show the apo state is least flexible in this region, but only slightly so. The

opposite trend is observed in the helical region at residues D50 to L61: the RMSF decreases with increasing residue number, and the apo case's RMSF is consistently 0.5 Å greater than the holo and half-saturated cases. For the cEF region, the half-saturated state has the largest RMSF, peaking at 2.07 ± 0.66 Å, followed by the apo state at 1.65 ± 0.29 Å and the holo state at 1.48 ± 0.92 Å. This trend of protein state and corresponding peak maxima matches that of the pEF hand, but unlike the former region, the differences for each protein case are not statistically significant.

1.3.3 Electrostatic scores assuming identical oxygen charges for backbone and side chain oxygens

We also show that the types of interactions with the protein play an important role in determining the strength of the electrostatic scores (Fig. 4B). When all the oxygens are assigned the same charge as the backbone oxygens, then the difference in the electrostatic scores between the pEF and cEF hands decrease significantly. The electrostatic score for the holo cEF hand with the backbone charges is -5.57, which is 1.75 less favorable than that of its counterpart in Fig. 4A. This new score is also much closer to that of the holo pEF hand with the difference being only 0.61 as opposed to 1.46 for the case above. These results suggest that the composition of oxygen atoms play an important role in effecting the binding affinity. Four of the seven oxygen atoms chelating with the Ca^{2+} ion in the pEF hand are backbone oxygens, whereas only one of the coordinating oxygen atoms is a backbone oxygen in the cEF hand. Since the side-chain oxygens have an increased negative charge, they have more favorable electrostatic interactions, and thus, would explain an improved binding affinity.

1.3.4 MM electrostatic energies versus Electrostatic scores

In order to validate out electrostatic score method, we calculated the MM electrostatic energy between the Ca^{2+} ion and the residues in the EF hand. Our results for these trials are shown in Fig. S2 and Table S3. The energetic trends

between the pEF and the cEF hands of the holo state match what was observed above in the electrostatic score calculations. The pEF hand has significantly less favorable MM electrostatic energies than the cEF hand, -168.0 ± 13.0 kcal/mol versus -577.1 ± 25.3 kcal/mol respectively, which agrees with what we determined from the electrostatic score calculations. These results agree with the experiments that show that Ca^{2+} ions have a stronger binding affinity to the cEF hand than the pEF hand (15, 16). The energetic trends for the cEF hand of the half-saturated versus fully saturated holo states are similar for both the MM electrostatic energy and the calculated electrostatic scores. The cEF hands have statistically similar energies for the half-saturated and holo states, -584.0 ± 21.3 kcal/mol versus -577.1 ± 25.3 kcal/mol respectively. This observation further supports the observation of non-cooperativity between the two hands since the absence of the Ca^{2+} ion in the pEF hand does not seem to affect the energetics of Ca^{2+} binding in the cEF hand. These data suggest that the electrostatic scores and MM electrostatic energies are in relative agreement.

1.3.5 β-sheet hydrogen bond between K31 in the pEF hand and G65 in the cEF hand

In Fig. S3, we compare MD simulations of the holo and apo states after 100 ns. It is notable that the shape of the EF hands and the adjoining β-sheet change significantly between the apo and holo states. In the holo state, G65 moves far from its position in the apo state because it is between N64 and D66, both of which coordinate with the Ca^{2+} ion. Thus, when the EF hands reorient themselves around the Ca^{2+} ion, the interaction is broken between K31 and G65 in order to form new interactions.

Table S3: Raw data and calculated average MM electrostatic energy [kcal/mol] (extracted from MM/PBSA calculations) between the Ca^{2+} ion and the residues in the respective EF hands for the half-saturated and fully saturated holo states. The pEF hand and cEF hand consist of residues S19 to E33 and D62 to E73, respectively. The respective standard deviations for the eight cases were calculated by AMBER's MM/PBSA program and are averaged over the course of the simulation.

Case	EF hand	Run	Chain	Average Electrostatic Energy [kcal/mol]
Half-Sat.	cEF	1	A	-602.4 ± 8.2
		1	B	-598.6 ± 10.6
		2	A	-597.0 ± 22.8
		2	B	-598.7 ± 31.7
		3	A	-540.0 ± 13.0
		3	B	-559.8 ± 16.6
		4	A	-579.3 ± 13.4
		4	B	-595.9 ± 8.2
			Mean	**-584.0 ± 21.3**
Holo	cEF	1	A	-594.4 ± 7.1
		1	B	-597.4 ± 9.0
		2	A	-592.4 ± 22.2
		2	B	-601.7 ± 9.7
		3	A	-532.4 ± 16.9
		3	B	-568.1 ± 26.5
		4	A	-540.7 ± 9.6
		4	B	-589.8 ± 7.8
			Mean	**-577.1 ± 25.3**
Holo	pEF	1	A	-163.9 ± 9.6
		1	B	-180.3 ± 22.4
		2	A	-170.0 ± 8.0
		2	B	-181.1 ± 11.0
		3	A	-185.2 ± 24.0
		3	B	-164.8 ± 9.8
		4	A	-150.2 ± 9.6
		4	B	-148.5 ± 8.3
			Mean	**-168.0 ± 13.0**

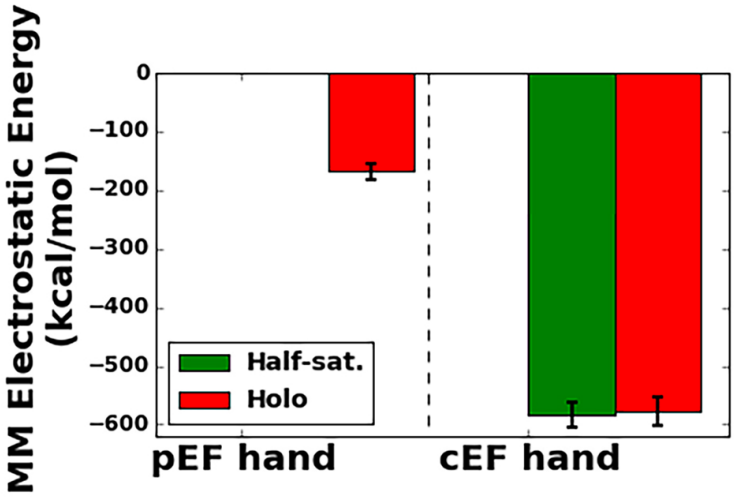

Figure S2: Calculated MM electrostatic energy (extracted from MM/PBSA calculations) between the Ca^{2+} ion and the residues in the respective EF hands for the half-saturated (green) and fully saturated holo (red) states averaged over quadruplicate simulations. The pEF hand and cEF hand consist of residues S19 to E33 and D62 to E73, respectively. Vertical error bars indicate the standard deviation of the eight mean electrostatic scores for two protein chains and the four simulation runs. The trends shown here for the MM electrostatic scores agree with those shown for the electrostatic scores in Fig. 4.

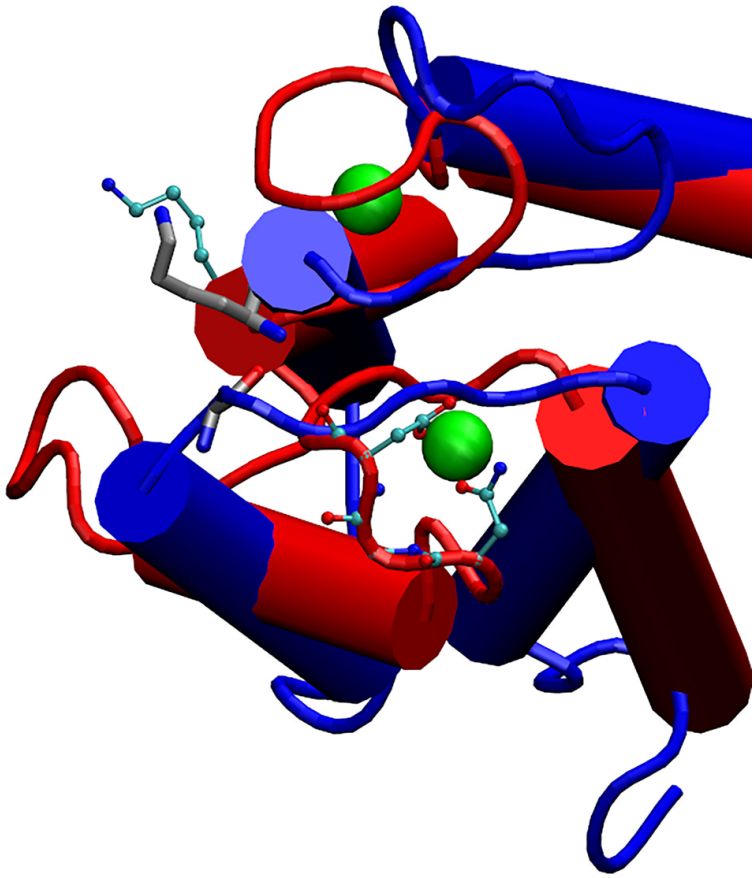

Figure S3: A comparison of the EF hands in chain A of the apo (blue) and the holo (red) forms of the S100A1 protein. K31 and G65 are shown in gray licorice for the apo case, and K31, N64, G65, and D66 are shown in cyan CPK for the holo case. Ca^{2+} ions are green.

1.3.6 Principle component analysis on the extended half-saturated cases

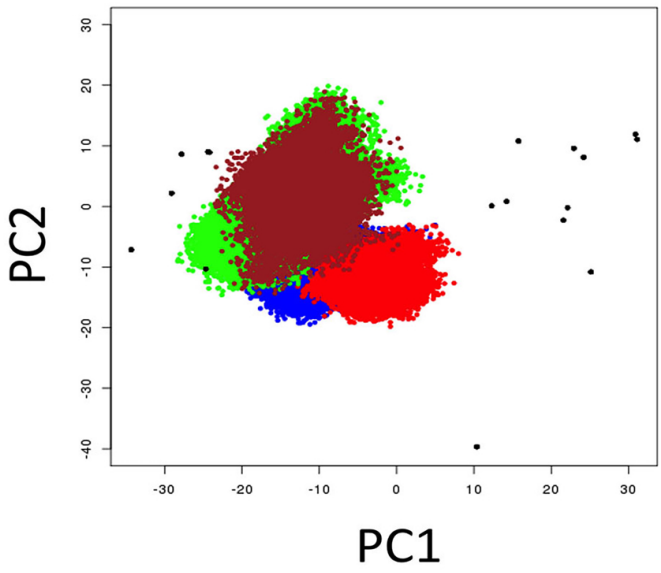

Figure S4: PCA for the four extended simulation runs of the half-saturated states.

Bibliography

1. Miyamoto, S., and P. A. Kollman, 1992. SETTLE: An analytical version of the SHAKE and RATTLE algorithm for rigid water models. *J. Comput. Chem.* 13:952–962. 1.1.1

2. Ryckaert, J. P., G. Ciccotti, and H. J. C. Berendsen, 1977. Numerical integration of cartesian equations of motion of a systerm with constratints: Molecular dynamics of N-alkanes. *J. Comput. Phys.* 23:327–341. 1.1.1

3. Berendsen, H. J. C., J. P. M. Postma, W. F. Vangunsteren, A. Dinola, and J. R. Haak, 1984. Molecular dynamics with coupling to an external bath. *J. Chem. Phys.* 81:3684–3690. 1.1.1

4. Darden, T., D. York, and L. Pedersen, 1993. Particle mesh Ewald: An N.log(N) method for Ewald sums in large systems. *J. Chem. Phys.* 98:10089–10092. 1.1.1

5. Kollman, P. A., I. Massova, C. Reyes, B. Kuhn, S. H. Huo, L. Chong, M. Lee, T. Lee, Y. Duan, W. Wang, O. Donini, P. Cieplak, J. Srinivasan, D. A. Case, and T. E. Cheatham, 2000. Calculating structures and free energies of complex molecules: Combining molecular mechanics and continuum models. *Acc. Chem. Res.* 33:889–897. 1.2

6. Gohlke, H., and D. A. Case, 2004. Converging free energy estimates: MM-PB(GB)SA studies on the protein-protein complex Ras-Raf. *J. Comput. Chem.* 25:238–250.

7. Hou, T., J. Wang, Y. Li, and W. Wang, 2011. Assessing the Performance of the Molecular Mechanics/Poisson Boltzmann Surface Area and Molecular Mechanics/Generalized Born Surface Area Methods. II. The Accuracy of Ranking Poses Generated From Docking. *J. Comput. Chem.* 32:866–877.

8. Miller, I., Bill R., J. McGee, T. Dwight, J. M. Swails, N. Homeyer, H. Gohlke, and A. E. Roitberg, 2012. MMPBSA.py: An Efficient Pro-

gram for End-State Free Energy Calculations. *J. Chem. Theory Comput.* 8:3314–3321. 1.2

9. Case, D., V. Babin, J. Berryman, R. Betz, Q. Cai, D. Cerutti, T. Cheatham III, T. Darden, R. Duke, H. Gohlke, A. Goetz, S. Gusarov, N. Homeyer, P. Janowski, J. Kaus, I. Kolossvary, A. Kovalenko, T. Lee, S. LeGrand, T. Luchko, R. Luo, B. Madej, K. Merz, F. Paesani, D. Roe, A. Roitberg, C. Sagui, R. Salomon-Ferrer, G. Seabra, C. Simmerling, W. Smith, J. Swails, R. Walker, J. Wang, R. Wolf, X. Wu, and P. Kollman, 2014. AMBER 14. 1.2

10. Nowakowski, M., L. Jaremko, M. Jaremko, I. Zhukov, A. Belczyk, A. Bierzyriski, and A. Ejchart, 2011. Solution NMR structure and dynamics of human apo-S100A1 protein. *J. Struct. Biol.* 174:391–399. S1

11. Zivkovic, M. L., M. Zareba-Koziol, L. Zhukova, J. Poznanski, I. Zhukov, and A. Wyslouch-Cieszynska, 2012. Post-translational S-nitrosylation is an endogenous factor fine tuning the properties of human S100A1 protein. *J. Biol. Chem.* 287:40457–40470. S1

12. Nowakowski, M., K. Ruszczynska-Bartnik, M. Budzinska, L. Jaremko, M. Jaremko, K. Zdanowski, A. Bierzynski, and A. Ejchart, 2013. Impact of calcium binding and thionylation of S100A1 protein on its Nuclear Magnetic Resonance-derived structure and backbone dynamics. *Biochemistry* 52:1149–1159. S1, S2, 1.3.2

13. Kekenes-Huskey, P., S. Lindert, and J. McCammon, 2012. Molecular basis of calcium-sensitizing and desensitizing mutations of the human cardiac troponin C regulatory domain: a multi-scale simulation study. *PLoS Comp. Biol.* 8:e1002777–e1002777. 1.3.2

14. Lindert, S., P. Kekenes-Huskey, G. Huber, L. Pierce, and J. McCammon, 2012. Dynamics and calcium association to the N-terminal regulatory domain of human cardiac troponin C: a multiscale computational study. *J. Phys. Chem. B* 116:8449–8459. 1.3.2

15. Goch, G., S. Vdovenko, H. Kozlowska, and A. Bierzynski, 2005. Affinity of S100A1 protein for calcium increases dramatically upon glutathionylation. *FEBS J.* 272:2557–2565. 1.3.2, 1.3.4

16. Wright, N. T., K. M. Varney, K. C. Ellis, J. Markowitz, R. K. Gitti, D. B. Zimmer, and D. J. Weber, 2005. The three-dimensional solution structure of Ca2+-bound S100A1 as determined by NMR spectroscopy. *J. Mol. Biol.* 353:410–426.